Supplementary Information for:

Iodide Oxidation by Ozone at the Surface of Aqueous Microdroplets

Alexander M. Prophet[1,2], Kritanjan Polley,[1,2] Gary J. Van Berkel[3], David T. Limmer[1,2,4,5] and Kevin R. Wilson[1,*]

[1]Chemical Sciences Division, Lawrence Berkeley National Laboratory, Berkeley, CA 94720

[2]Department of Chemistry, University of California, Berkeley, CA 94720

[3]Van Berkel Ventures, LLC, Oak Ridge, TN 37830

[4]Materials Science Division, Lawrence Berkeley National Laboratory, Berkeley, California 94720

[5]Kavli Energy NanoScience Institute, Berkeley, California 94720

*Correspondence to krwilson@lbl.gov

Contents

SI-1: Model reaction steps

SI-2: OPSI-MS droplet concentration response, example mass spectra, and iodate formation kinetics

SI-3: Molecular Dynamics simulations: methodology, results, and discussion

SI-4: Diffusional length scales

SI-5: Model parameter sensitivity

SI-6: Model pH-dependence test

SI-7: Simulated product distributions

SI-1: Model reaction steps

The complete set of elementary steps used in the model and implemented in Kinetiscope© are shown in Table S1. As outlined in the main text, kinetic steps can occur within the surface or bulk compartment (steps labeled S or B, respectively in Table S1). Diffusion steps are labeled D. Each labeled step is shown along with rate or diffusion coefficients used for the physical adsorption, chemical reactions, diffusion, and evaporative steps. References for literature equilibrium coefficients, rate constants, diffusion coefficients, and Henry's law constants are provided in the right-most column.

Table S1: Elementary reaction steps, rate and diffusion coefficients used in the Kinetiscope© simulations. Reaction steps that occur in the surface compartment, diffusion coefficients for the transfer of species between surface and bulk compartments, and bulk compartment steps are labeled by S, D, and B respectively. Literature references for the rate coefficients, diffusion constants, and Henry's Law constants are also provided.

#	Step	Rate coefficient	Reference
S1	$O_{3(g)} \underset{k_{diff}}{\overset{k_{diff}}{\rightleftarrows}} O_{3(diff)}$	$k_{diff} = 1.6 \times 10^8 \ s^{-1}$	see sections IV.A.(ii) & SI-4
S2	$O_{3(diff)} + site_{O_3} \underset{k_{des}}{\overset{k_{ads}}{\rightleftarrows}} O_{3(ads)}$	$k_{ads} = 3.31 \times 10^{-11} \ cm^3 \cdot molec.^{-1} \cdot s^{-1}$ $k_{des} = 1.93 \times 10^{10} \ s^{-1}$	see sections IV.A.(i) & SI-3
S3	$O_{3(ads)} \underset{k_{desolv}}{\overset{k_{solv}}{\rightleftarrows}} O_{3(b)} + site_{O_3}$	$k_{solv} = 1.90 \times 10^8 \ s^{-1}$ $k_{desolv} = 2.25 \times 10^{-12} \ cm^3 \cdot molec.^{-1} \cdot s^{-1}$	see sections IV.A.(i) & SI-3
S4	$I^-_{(ads)} \underset{k_{desolv}}{\overset{k_{solv}}{\rightleftarrows}} I^-_{(b)} + site_I$	$k_{solv} = 1 \times 10^3 \ s^{-1}$ $k_{desolv} = 5.35 \times 10^{-19} \ cm^3 \cdot molec.^{-1} \cdot s^{-1}$	1,2
S5	$IO^-_{(ads)} \underset{k_{desolv}}{\overset{k_{solv}}{\rightleftarrows}} IO^-_{(b)} + site_I$	$k_{solv} = 1 \times 10^3 \ s^{-1}$ $k_{desolv} = 5.35 \times 10^{-19} \ cm^3 \cdot molec.^{-1} \cdot s^{-1}$	1,2
S6	$IO^-_{2(ads)} \underset{k_{desolv}}{\overset{k_{solv}}{\rightleftarrows}} IO^-_{2(b)} + site_I$	$k_{solv} = 1 \times 10^3 \ s^{-1}$ $k_{desolv} = 5.35 \times 10^{-19} \ cm^3 \cdot molec.^{-1} \cdot s^{-1}$	1,2
S7	$IO^-_{3(ads)} \underset{k_{desolv}}{\overset{k_{solv}}{\rightleftarrows}} IO^-_{3(b)} + site_I$	$k_{solv} = 1 \times 10^3 \ s^{-1}$ $k_{desolv} = 5.35 \times 10^{-19} \ cm^3 \cdot molec.^{-1} \cdot s^{-1}$	1,2
S8	$I_{2(ads)} \underset{k_{desolv}}{\overset{k_{solv}}{\rightleftarrows}} I_{2(b)} + site_I$	$k_{solv} = 1 \times 10^3 \ s^{-1}$ $k_{desolv} = 5.35 \times 10^{-19} \ cm^3 \cdot molec.^{-1} \cdot s^{-1}$	1,2
S9	$HOI_{(ads)} \underset{k_{desolv}}{\overset{k_{solv}}{\rightleftarrows}} HOI_{(b)} + site_I$	$k_{solv} = 1 \times 10^3 \ s^{-1}$ $k_{desolv} = 5.35 \times 10^{-19} \ cm^3 \cdot molec.^{-1} \cdot s^{-1}$	1,2

S10	$I^-_{3(ads)} \underset{k_{desolv}}{\overset{k_{solv}}{\rightleftharpoons}} I^-_{3(b)} + site_I$	$k_{solv} = 1 \times 10^3 \text{ s}^{-1}$ $k_{desolv} = 5.35 \times 10^{-19} \ cm^3 \cdot molec.^{-1} \cdot s^{-1}$	1,2
S11	$I^-_{(ads)} + O_{3(ads)} \underset{k_r}{\overset{k_f}{\rightleftharpoons}} IOOO^-_{(ads)} + site_{O_3}$	$k_f = 2 \times 10^{-12} \ cm^3 \cdot molec.^{-1} \cdot s^{-1}$ $k_r = 3.6 \times 10^4 \text{ s}^{-1}$	3 see note§
S12	$IOOO^-_{(ads)} + H^+ \xrightarrow{k_f} HOI_{(ads)}$	$^\dagger k_f = 1.66 \times 10^{-10} \ cm^3 \cdot molec.^{-1} \cdot s^{-1}$	§
S13	$IOOO^-_{(ads)} \xrightarrow{k_f} IO^-_{(ads)}$	$k_f = 2.2 \times 10^2 \text{ s}^{-1}$	§
S14	$IO^-_{(ads)} + O_{3(ads)} \xrightarrow{k_f} IO^-_{2(ads)} + site_{O_3}$	$k_f = 1.66 \times 10^{-11} \ cm^3 \cdot molec.^{-1} \cdot s^{-1}$	4 see note $^\int$
S15	$IO^-_{2(ads)} + O_{3(ads)} \xrightarrow{k_f} IO^-_{3(ads)} + site_{O_3}$	$k_f = 1.66 \times 10^{-11} \ cm^3 \cdot molec.^{-1} \cdot s^{-1}$	4 see note $^\int$
S16	$IO^-_{(ads)} + H^+ \underset{k_r}{\overset{k_f}{\rightleftharpoons}} HOI_{(ads)}$	$^\dagger k_f = 1.66 \times 10^{-10} \ cm^3 \cdot molec.^{-1} \cdot s^{-1}$ $k_r = 1.58 \text{ s}^{-1}$	5,6 see note†
S17	$HOI_{(ads)} + I^-_{(ads)} \underset{k_r}{\overset{k_f}{\rightleftharpoons}} I_2OH^-_{(ads)} + site_I$	$k_f = 6.64 \times 10^{-17} \ cm^3 \cdot molec.^{-1} \cdot s^{-1}$ $k_r = 1.34 \times 10^2 \text{ s}^{-1}$	7
S18	$I_2OH^-_{(ads)} + H^+ \underset{k_r}{\overset{k_f}{\rightleftharpoons}} I_{2(ads)}$	$^\dagger k_f = 3.32 \times 10^{-11} \ cm^3 \cdot molec.^{-1} \cdot s^{-1}$ $k_r = 3.2 \text{ s}^{-1}$	7
S19	$HOI_{(ads)} + I^-_{(ads)} \underset{k_r}{\overset{k_f}{\rightleftharpoons}} I_{2(ads)} + OH^- + site_I$	$k_f = 3.5 \times 10^{-18} \ cm^3 \cdot molec.^{-1} \cdot s^{-1}$ $^\dagger k_r = 1.16 \times 10^{-16} \text{ s}^{-1}$	8
S20	$I_{2(ads)} + I^-_{(ads)} \leftrightarrow I^-_{3(ads)} + site_I$	$^+ k_f = 1 \times 10^{-15} \ cm^3 \cdot molec.^{-1} \cdot s^{-1}$ $k_r = 8.64 \times 10^2 \text{ s}^{-1}$	9
S21	$I_{2(ads)} \xrightarrow{k_{evap}} I_{2(g)} + site_I$	$k_{evap} = 10^5 \text{ s}^{-1}$	10
S22	$HOI_{(ads)} \xrightarrow{k_{evap}} HOI_{(g)} + site_I$	$k_{evap} = 1.76 \times 10^3 \text{ s}^{-1}$	11
D1	$I^-_{(b)}$	$D = 1.53 \times 10^{-5} \text{ cm}^2 \cdot s^{-1}$	12
D2	$IO^-_{(b)}$	$D = 1.53 \times 10^{-5} \text{ cm}^2 \cdot s^{-1}$	12
D3	$IO^-_{2(b)}$	$D = 1.53 \times 10^{-5} \text{cm}^2 \cdot s^{-1}$	12
D4	$IO^-_{3(b)}$	$D = 1.53 \times 10^{-5} \text{ cm}^2 \cdot s^{-1}$	12
D5	$I_2OH^-_{(b)}$	$D = 1.53 \times 10^{-5} \text{ cm}^2 \cdot s^{-1}$	12
D6	$I^-_{3(b)}$	$D = 1.07 \times 10^{-5} \text{ cm}^2 \cdot s^{-1}$	13
D7	$I_{2(b)}$	$D = 1.15 \times 10^{-5} \text{ cm}^2 \cdot s^{-1}$	14
D8	$HOI_{(b)}$	$D = 1.53 \times 10^{-5} \text{ cm}^2 \cdot s^{-1}$	12
D9	$O_{3(b)}$	$D = 1.76 \times 10^{-5} \text{ cm}^2 \cdot s^{-1}$	15

B1	$I^-_{(b)} + O_{3(b)} \underset{k_r}{\overset{k_f}{\rightleftharpoons}} IOOO^-_{(b)}$	$k_f = 2 \times 10^{-12}\ cm^3 \cdot molec.^{-1} \cdot s^{-1}$ $k_r = 3.6 \times 10^4\ s^{-1}$	3 see note§
B2	$IOOO^-_{(b)} + H^+ \xrightarrow{k_f} HOI_{(b)}$	$^\dagger k_f = 1.66 \times 10^{-10}\ cm^3 \cdot molec.^{-1} \cdot s^{-1}$	$\S$
B3	$IOOO^-_{(b)} \xrightarrow{k_f} IO^-_{(b)}$	$k_f = 2.2 \times 10^2\ s^{-1}$	$\S$
B4	$IO^-_{(b)} + O_{3(b)} \xrightarrow{k_f} IO^-_{2(b)}$	$k_f = 2.65 \times 10^{-15}\ cm^3 \cdot molec.^{-1} \cdot s^{-1}$	6
B5	$IO^-_{2(b)} + O_{3(b)} \xrightarrow{k_f} IO^-_{3(b)}$	$k_f = 2.65 \times 10^{-15}\ cm^3 \cdot molec.^{-1} \cdot s^{-1}$	6
B6	$IO^-_{(b)} + H^+ \underset{k_r}{\overset{k_f}{\rightleftharpoons}} HOI_{(b)}$	$^\dagger k_f = 1.66 \times 10^{-10}\ cm^3 \cdot molec.^{-1} \cdot s^{-1}$ $k_r = 1.58\ s^{-1}$	5,6 see note†
B7	$HOI_{(b)} + I^-_{(b)} \underset{k_r}{\overset{k_f}{\rightleftharpoons}} I_2OH^-_{(b)}$	$k_f = 6.64 \times 10^{-17}\ cm^3 \cdot molec.^{-1} \cdot s^{-1}$ $k_r = 1.34 \times 10^2\ s^{-1}$	7
B8	$I_2OH^-_{(b)} + H^+ \underset{k_r}{\overset{k_f}{\rightleftharpoons}} I_{2(b)}$	$^\dagger k_f = 3.32 \times 10^{-11}\ cm^3 \cdot molec.^{-1} \cdot s^{-1}$ $k_r = 3.2\ s^{-1}$	7
B9	$HOI_{(b)} + I^-_{(b)} \underset{k_r}{\overset{k_f}{\rightleftharpoons}} I_{2(b)} + OH^-$	$k_f = 3.5 \times 10^{-18}\ cm^3 \cdot molec.^{-1} \cdot s^{-1}$ $^\dagger k_r = 1.16 \times 10^{-16}\ s^{-1}$	8
B10	$I_{2(b)} + I^-_{(b)} \underset{k_r}{\overset{k_f}{\rightleftharpoons}} I^-_{3(b)} + site_I$	$^+ k_f = 1 \times 10^{-15}\ cm^3 \cdot molec.^{-1} \cdot s^{-1}$ $k_r = 8.64 \times 10^2\ s^{-1}$	9

§As discussed in main text, forward rates for steps S11, S16, B2, and B6 utilize a diffusion limitation assumption. Rate coefficient k_r for step S11 and k_f for step S13 (and corresponding bulk steps B1 & B3) are treated as adjustable parameters in the model, yielding a single pair that agrees with experimental data.

$^\int$Rate coefficients from gas-phase measurements are faster than liquid-phase diffusion limit. Therefore, we estimate the rate to be equal to an approximate liquid-diffusion limited rate of $10^{10}\ M^{-1}\ s^{-1}$.

†[H$^+$] and [OH$^-$] are not defined explicitly in the simulations, where instead a pseudo-first order rate constant (e.g. $k \cdot$ [H$^+$]) is used to simulate reactions in solution assuming constant [H$^+$] and [OH$^-$].

$^+$Literature rate coefficients for the forward and reverse directions of this equilibrium are both 10^4 larger than coefficients used here. Because such a rapid equilibrium creates lengthy simulations times, the absolute rates have been diminished. However, model sensitivities tests have shown simulation results are insensitive to these rate coefficients above their presented values.

SI-2: OPSI-MS droplet concentration response, example mass spectra, iodate formation kinetics

In Fig. S1, the iodide peak area detected by the OPSI is compared against droplet solution concentration to analyze the linearity of droplet response. Measurements of peak area vs. concentration are compared to measurements using an internal standard ($NaClO_3$). In both cases, a high degree of linearity between droplet signal and concentration is observed. Slight deviations for total peak area are observed, likely due to variation in droplet radius between measurements on the order of ±1 μm, a result of slightly different water activities between conditions studied (NaCl concentrations adjusted accordingly to initial solution as to maintain constant water activity).
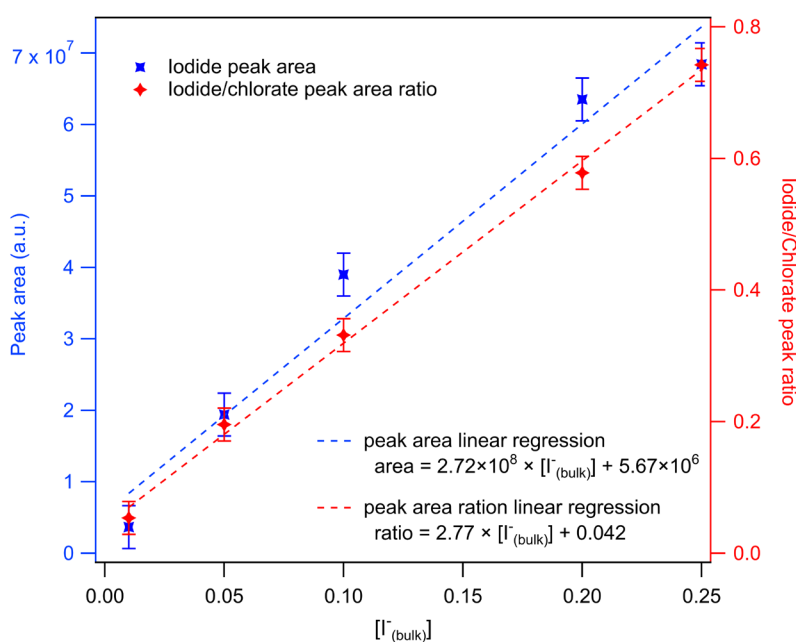

Fig. S1: Iodide peak area vs concentration to observe droplet response using the open-port sampling interface. Peak area ratios of iodide to an internal standard (ClO_3^-) are also provided to demonstrate linearity of both approaches.

Mass spectra for typical droplet detection events are included in Fig. S2 demonstrating the overall intensity of the iodide anion signal before reaction, and the decreased signal after oxidation by ozone. This particular example shows production of IO_3^- at m/z = 174 under strong basic conditions after ~35 minutes of exposure to a 1.6 ppm $[O_3]$ flow. Typical background ions observed by the mass spectrometer are labeled in the "reacted" spectrum where the overall iodide signal is diminished. These background ions ($C_3H_5O_3^-$ m/z = 89.0, $C_2H_5O_3^-$ m/z = 77.0, $C_2H_3O_3^-$ m/z = 75.0) are small organics that originate either from dilute impurities in the methanol used as the OPSI solvent, or simply from the interaction between the laboratory air and the electrospray plume. These background peaks are also present in the unreacted

spectrum in Fig. S2 but are dwarfed by the intensity of the iodide peak at m/z = 126.9. While small impurities are commonly observed in all of our experiments, these species have not been observed to impact the kinetic measurements. Formation kinetics of IO_3^- are also provided in Fig. S3 for three ozone concentrations < 1 ppm. Notably, we observe the production of IO_3^- to diminish with decreasing O_3, an effect not observed in the kinetic simulations. The origin of this effect is unknown, but we speculate this is possibly due to I_2 production and evaporation when the oxidation rate of IO^- becomes sufficiently slow under low $[O_3]$.
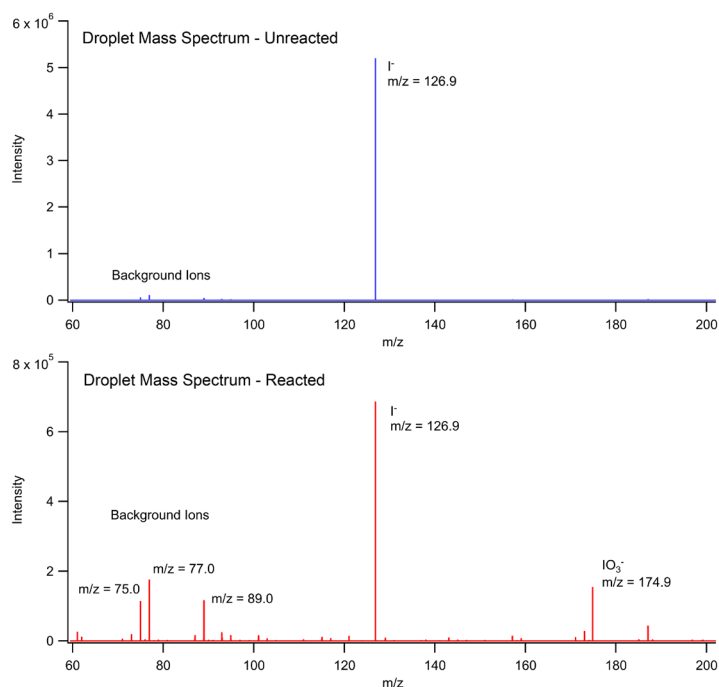

Fig. S2: Mass spectra for unreacted and reacted microdroplets containing NaI at pH 13. Reacted droplet spectrum results from 35 minutes of oxidation using $[O_3] = 1.6$ ppm. In this case, IO_3^- is observed as a soluble product in the spectrum.
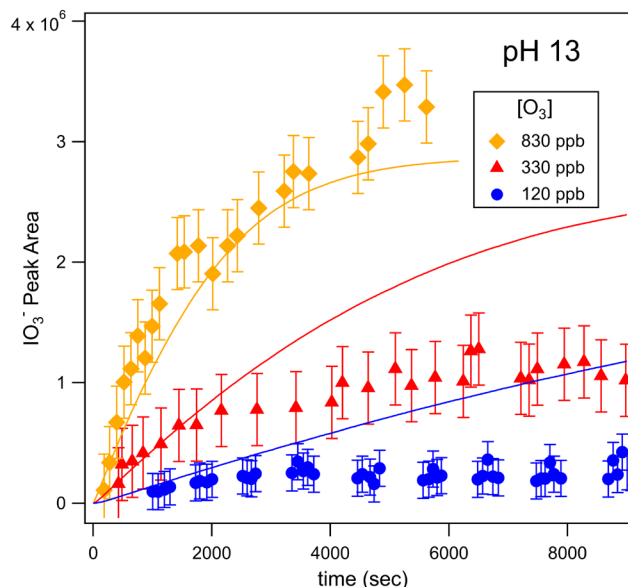
Fig. S3: Experiment and simulation results showing production of IO_3^- for a series of sub-ppm $[O_3]$ with initial droplet pH =13 and a droplet radius of 24 μm. Total ion signal at m/z 174 is observed to decrease as $[O_3]$ decreases, indicating a change in the surface mechanism of I^- oxidation not predicted by the model results.

SI-3: Molecular Dynamics simulations: methodology, results, and discussion

A. Free Energy Profiles

We used a classical polarizable force field to model the air water interface. A water slab with 768 water molecules at 300 K in a box of size a box of size $24.8 \times 24.8 \times 111.76$ Å^3 was used to represent an aqueous droplet where the larger dimension, denoted the z-axis, is perpendicular to the interface. A periodic boundary condition was applied in all directions. Water, ions and ozone were simulated with a polarizable force field in conjunction with SWM4-NDP[16] as the water model. To use a large time step of 1 fs, we employed a rigid body dynamics for the water and ozone.[17] The non-bonded pair interactions were described with a '12-6' Lennard-Jones model

$$U_{LJ} = \sum_{i,j} 4\epsilon_{ij} \left[\left(\frac{\sigma_{ij}}{r_{ij}} \right)^{12} - \left(\frac{\sigma_{ij}}{r_{ij}} \right)^6 \right], \qquad \text{Eq. (S1)}$$

where r_{ij} is the distance between sites i and j and σ_{ij} and ϵ_{ij} are Lennard-Jones parameters. These parameters are summarized in Table S2. A Lorentz-Berthelot mixing rule was used where $\sigma_{ij} = (\sigma_{ii} + \sigma_{jj})/2$ and $\epsilon_{ij} = \sqrt{\epsilon_{ii}\epsilon_{jj}}$. A Drude[18] oscillator model was used to replicate polarization in the

simulation. A spring constant, k_D, of 1000 kcal mol^{-1} Å^{-2} was set for all the Drude oscillators in system,[19] which determines the charge q_D that the Drude particle must carry to produce the correct polarizability through the relation $\zeta = q_D^2/k_D$.

Table S2: The force field parameters used in MD simulation. The water force field parameters are taken from Lamoureux et al.,[16] the ozone force field from Vieceli et al.,[20] and the alkali halide force field from Dang et al.[21] For an ozone molecule, $r_{eq}(O_{center} - O_{side}) = 1.28$ Å, and $\theta_{eq} = 116.7°$.

Species	Atom	ϵ(kcal mol^{-1})	σ(Å)	ζ, Polarizability (Å^3)
H$_2$O	H	0.0000	0.0000	0.0000
	O	0.2109	3.1839	0.9783
O$_3$	O$_{center}$	0.1560	3.2037	0.9500
	O$_{side}$	0.1560	3.2037	0.9500
Na$^+$	Na	0.1000	2.2718	0.2400
Cl$^-$	Cl	0.1000	4.3387	3.6900
I$^-$	I	0.1000	5.1245	6.9200

An extended Lagrangian dynamics, with velocity-Verlet[22] time integration scheme, was used in which a small mass and kinetic energy are attributed to the Drude particles. The amplitude of the Drude oscillator was controlled with a low temperature thermostat (1 K) acting in the local center-of-mass frame of each atom-Drude pair.[19] Thole damping[23] was used to modulate the electrostatic interaction between particles and induced dipoles. A particle-particle-particle-mesh method[24] was used as the long range Coulomb interaction solver. The force field was symmetrized with the procedure outlined by Dodin & Geissler.[25] The Lennard-Jones interactions were truncated and shifted at a distance of 12 Å.

Free energy for transferring an ozone molecule through the air-water interface, $\Delta G(z)$ was computed using umbrella sampling method.[26] In all simulations, ozone was restrained at a fixed distance from the center of mass of the water slab with a harmonic bias of the form $k_z(z - z_0)^2$ with $k_z = 4$ kcal mol^{-1} Å^{-2} as the spring constant of the bias and z_0 its center. A total of 71 windows, with z_0 spaced 1 Å were used between -35 Å and 35 Å along z. Each window was run for 15 ns after 1 ns equilibration. The different umbrellas were used together with the Weighted Histogram Analysis

Method.[27] The free energy profile was referenced relative to the vacuum, such that far from the interface, $\Delta G(z) = 0$.

Fig. S4 presents the free energy profile for ozone with sodium halide salts in the solution, also found in the main text Fig. 4(B), and the free energy profile for iodide in the same simulated solution. The density profiles for aqueous ions and ozone are presented below in Fig. S5 where both the iodide ion and ozone exhibit a preference for the interfacial region. The Henry's law constants that determine mass partitioning between the gas and surface, H_{cc}^{gs}, the surface and bulk, H_{cc}^{sb}, and gas and bulk, H_{cc}^{gb} are computable form the free energy profile. We define the free energy difference between the gas and surface as ΔG_{gs} where the surface is taken to be the minimum of the free energy, near $z \sim 20$ Å, and the vapor at taken at large z. The resultant Henry's law constant is then $H_{cc}^{gs} = \exp(-\Delta G_{gs}/k_B T) = 9.3$ where k_B is Boltzmann's constant and T is the absolute temperature. Analogously, we define the free energy difference between the surface and bulk as ΔG_{sb} where the bulk free energy is taken as the plateau value of $\Delta G(z)$ in the interior of the slab, $z = 0$. The resultant Henry's law constant is then $H_{cc}^{sb} = \exp(-\Delta G_{sb}/k_B T) = 0.0156$. This renders the Henry's law constant from the gas to the bulk, $H_{cc}^{gb} = H_{cc}^{gs} H_{cc}^{sb} = 0.145$.
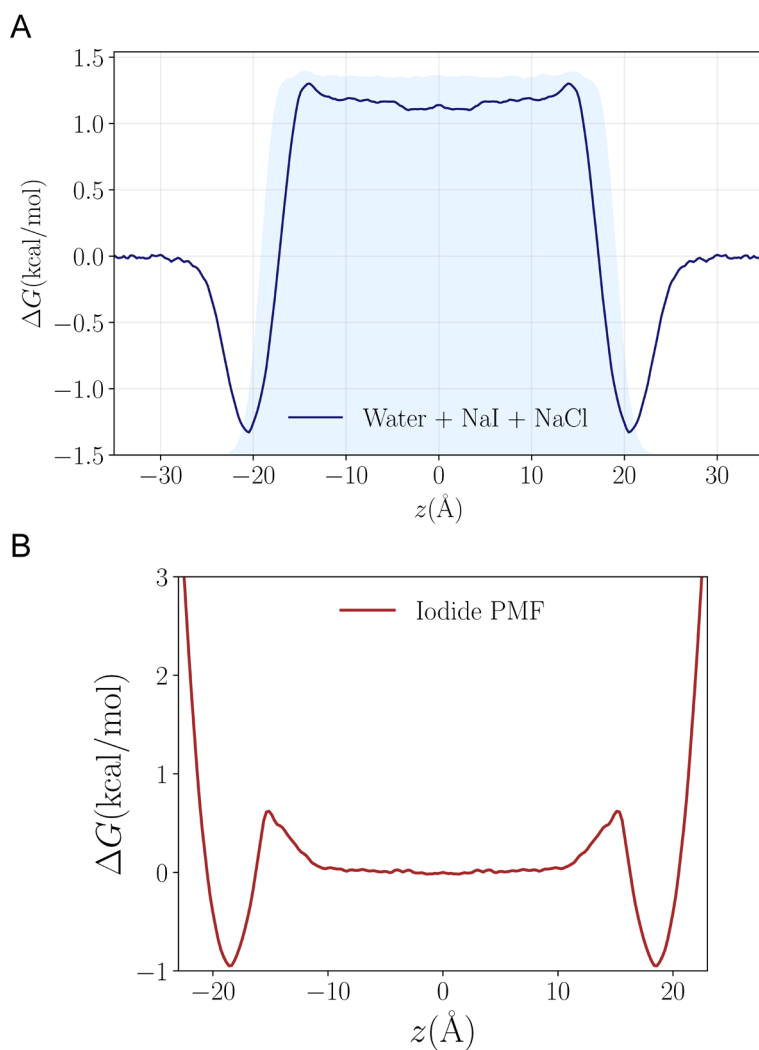
Fig. S4: (A) The free energy profile for transferring an ozone molecule through a water slab with 0.28 M NaI and 0.84 M NaCl is displayed. The shaded blue region shows the (scaled and shifted) water density profile. (B) The free energy profile for transferring an iodide anion through a similar water slab. A cutoff for the free energy approaching the gas-phase is 3 kcal mol^{-1}.
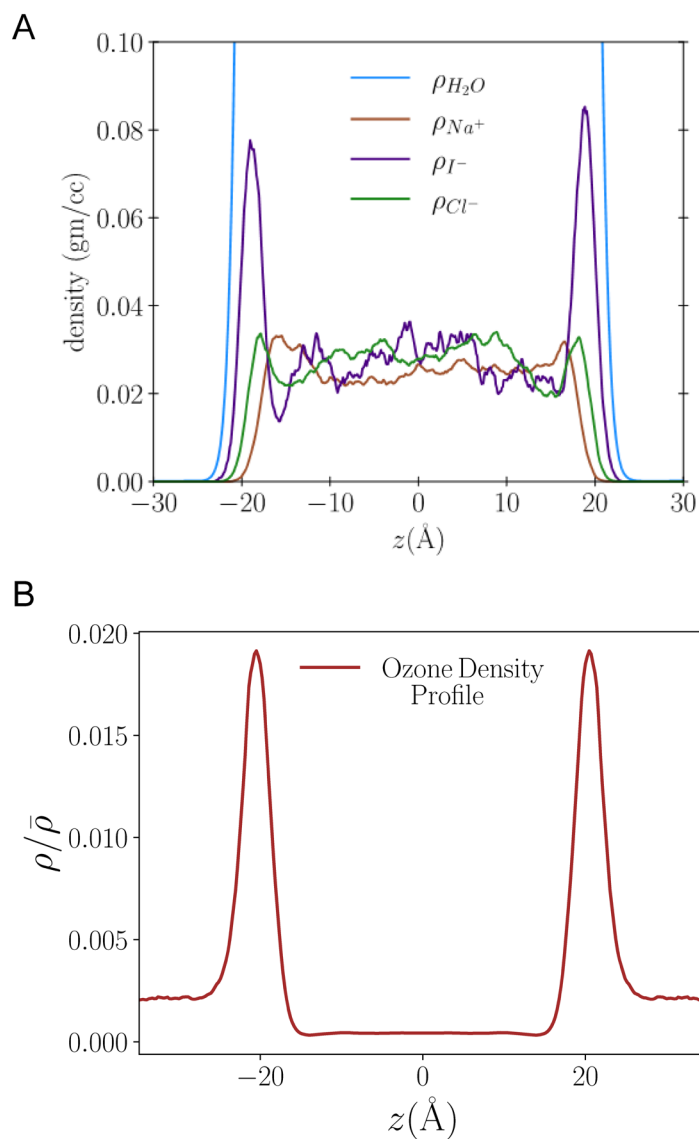
Fig. S5: (A) The density profiles of the ions are presented. The blue line shows the water density profile. The brown, purple, and green curves represent Na^+, I^-, and Cl^- ion densities, respectively. (B) Normalized density profile of ozone through a water slab with 0.28 M NaI and 0.84 M.

B. Solvation and Desorption Rates

We define the mass accommodation coefficient (α) as the fraction of collisions of the gas phase species with the interface that results in the transport of the gas phase particle into the condensed phase. The accommodation coefficient can be written as

$$\alpha = \frac{k_{solv}}{k_{solv} + k_{des}},$$

Eq. (S2)

where k_{des} and k_{solv} are the rate of desorption and rate of solvation, respectively, from interface. This expression is valid in the limit of unit sticking coefficient (σ) and rapid thermalization relative to the absorption and desorption process. We have computed these rates from by propagating an effective Langevin equation parameterized from our explicit molecular dynamics simulations,

$$m\dot{v} = -m\gamma(z)v + f(z) + \sqrt{2m\gamma(t)k_B T}\eta(t), \qquad \text{Eq. (S3)}$$

where m is the mass of the particle, v and $\gamma(z)$ (γ has a unit of inverse time) are the velocity and friction coefficient, respectively. In general, the friction is a function of the coordinate, z. We have evaluated using a procedure to be described elsewhere, yielding a functional form $\gamma(z) \sim \left(\tanh(w(-sign(z)z + s))\right)^n$ with $w = 0.2, s = 19.76,$ and $n = 2.34$. $f(z)$ is the force acting on the particle that is obtained from the free energy profiles in Fig. 4(B) as $-\partial\Delta G/\partial z$. k_B is the Boltzmann constant and T is the absolute temperature. $\eta(t)$ is the δ-correlated Gaussian noise with properties $\langle\eta(t)\rangle = 0$ and $\langle\eta(t)\eta(t')\rangle = \delta(t - t')$ where $\langle \cdots \rangle$ is a statistical average. The dot in Eq. (S3) indicates a time derivative. The free energy profile is obtained from molecular dynamics simulation. We adopt the methods detailed in Farago & Grønbech-Jensen[28] for propagating Langevin equation with a coordinate dependent friction function.

To determine the desorption or solvation rates, we compute the fraction of trajectories entering the gas phase or bulk phase as a function of time starting from the interfacial region where trajectories are generated with Eq. (S3). The boundaries of the interface, with the bulk solution and with the gas phase, are set where the free energy profile in Fig. 4(B) becomes flat in that given side. Indicator functions (h_r) are used to determine location of a trajectory in different regions, namely bulk liquid phase (b), interface (s), and gas phase (g). From the form of $\Delta G(z)$, for one side of the slab, we take the bulk as $z < 14.5$, the interface as $14.5 < z < 27$ and the vapor as $z > 27$. The rates are then determined by fitting.

$$\chi_r = \frac{\langle h_r(t)h_s(0)\rangle}{\langle h_s(0)\rangle}, \qquad \text{Eq. (S4)}$$

$$\chi_r(z) = \begin{cases} 1, & \text{if } z(t) \in r = \{b, s, g\} \\ 0, & \text{otherwise} \end{cases},$$

where $\chi_r(t)$ is a normalized side-side correlation function that determines what fraction of trajectories has entered or left a given region at a given time with an exponential. The side-side correlation functions for desorption and solvation processes are shown in Fig. **S6**. The desorption rate is obtained by fitting the initial rise of the desorption correlation function with an exponential. This value agrees nicely with the

desorption rate obtained from a steady state flux calculation. The ratio of desorption to solvation by examining fraction of density entering the bulk phase compared to the fraction entering the vapor phase starting from the interface region. Also, the solvation rate can be obtained in a similar way like desorption by fitting the initial rise of the correlation function with an exponential. These two results are in close agreement. The mass accommodation coefficient of ozone for this system can be computed from Eq. (S2) which gives a value of $\alpha = 0.0097$. The solvation and desorption rates are extracted from Fig. **S6** are $1.90 \times 10^8 \text{ s}^{-1}$ and $1.93 \times 10^{10} \text{ s}^{-1}$, respectively.
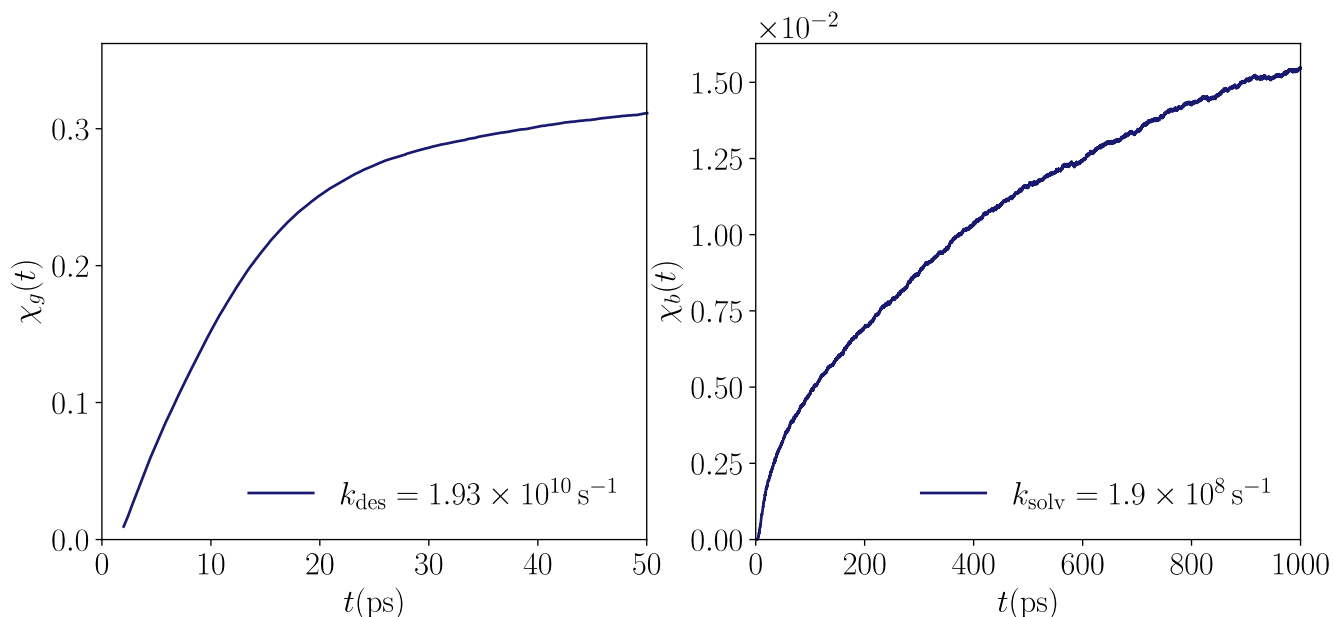

Fig. S6: The side-side correlation functions are plotted above. The rate of desorption and solvation are extracted by fitting the early rise in the correlation function with an exponential function of the form $c_1 - c_2 e^{-kt}$ ($c_1, c_2 > 0$) where k is the rate for the process. The initial position was set at the minima of the free energy profile. The left and right column represent the autocorrelation function for desorption and solvation processes, respectively. Rates are reported in s^{-1}.
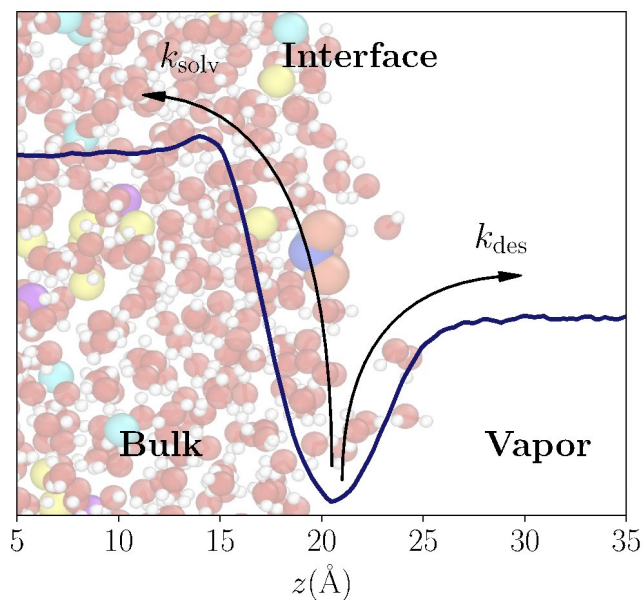
Fig. S7: A diagrammatic representation of the three regions, namely bulk, interface, and vapor, as used in the calculation of solvation and desorption rates.

SI-4: Diffusional length scales

Characteristic lengths for ozone diffusion and adsorption in the gas-phase are introduced in the modeling description section IV.A.(ii). Here we provide a sketch summarizing these lengths relative to an example droplet radius. While the diffusion length L_{diff} denotes the characteristic size of the chemical gradient by loss of O_3 on the droplet surface, the adsorption length L_{ads} denotes the size of the gas volume directly depleted by the kinetic adsorption equilibrium (step A1 in Table S1). Equivalently, one may conceptualize the volume defined by L_{ads} as the gas-volume that contains the same number of O_3 as the droplet surface at equilibrium. The upper limit for diffusion in the present model can then be constructed as diffusion over the length L_{diff} into the volume defined by L_{ads}.
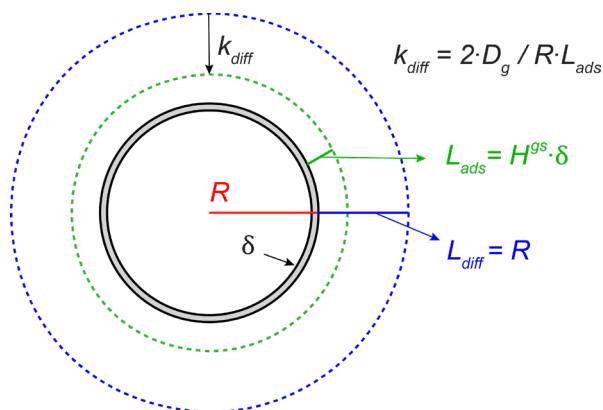
Fig. S8: Illustration of relevant length scales for gas-phase diffusion and a kinetic description of adsorption and diffusion.

SI-5: Model parameter sensitivity

Due to the large number of rate coefficients in the model framework used, we do not include a comprehensive sensitivity test for all coefficients but highlight what results from our work suggest are the main sensitivities in the model. Perhaps the largest uncertainties in the model are the solvation and desolvation rates of solutes in solution. The ratio of these rates, equal to the Langmuir equilibrium coefficient, is less uncertain given the simulated interfacial ion-densities provided in SI-3 and previous measurements of iodide surface concentrations. To the best of our knowledge, however, no measurements exist for absolute rates of surface-solvation or desolvation for the anions considered. Therefore, in the present modeling approach, we aim to choose absolute rates of k_{solv} and k_{desolv} of a large enough magnitude such that any sensitivity to the absolute values is lost. A brief illustration in Fig. S2 demonstrates that an example set of k_{solv}/k_{desolv} for I$^-$ that becomes too small will alter the model kinetics. This results from overlapping timescales of ion-desolvation and reaction under the particular reaction conditions. We generally assume that a reaction depletion of ions at the interface is non-physical under these conditions. This in turn derives from an assumption that rates of ion-replenishment at the interface occur on a timescale faster than reaction.
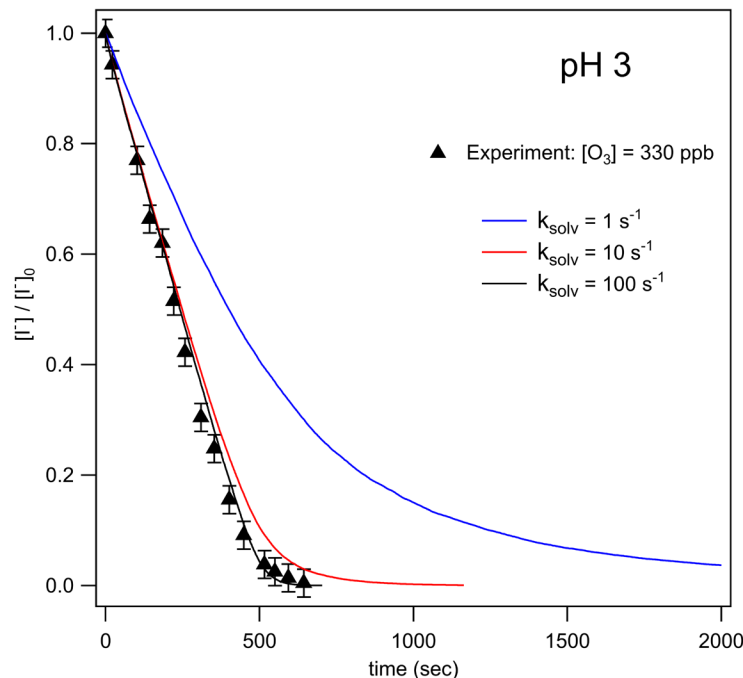
Fig. S9: Simulation results compared to experiment for a pH 3 droplet exposed to 330 ppb [O_3]. Results from scaling the k_{solv} and k_{desolv} rates are shown to display sensitivity to the absolute rates. Simulation results appear greatly sensitive to the absolute rates below $k_{solv} = 10$ s^{-1}. Above $k_{solv} = 10$ s^{-1}, the sensitivity quickly drops off and the kinetics remain approximately constant. Note that in each comparison case, k_{desolv} is scaled by the same factor as k_{solv}.

Similar sensitivity tests were also performed for the absolute rate coefficients embedded in the I_3^- equilibrium and I_2OH^- equilibrium, with an analogous finding that the simulation results are unchanged by increasing absolute rate coefficients. Since each of these equilibrium systems was tested individually while keeping the others constant, we note there may be additive effects that will go unobserved unless all equilibria were simulated using the literature forward and reverse rates. However, we expect any differences in a fully simulated case to be relatively small from the present simulations since no obvious deviations were observed while testing the sensitivity of individual equilibria.

SI-6: Model pH test

Model results suggest the pH dependence observed from experiment is a compound effect of pH dependent reaction pathways that consume iodide and the surface reaction rate. In this section we show the effect of the bulk and surface components. Removing the direct pH dependence of the surface reaction can be observed by simply replacing the 3-step surface mechanism (see main text Fig. 5B) and reaction R1-R3) with a 1-step bimolecular rate expression, as has been observed in the gas phase:

S16

$$I^- + O_3 \rightarrow IO^- + O_2 \qquad\qquad (SR1)$$

To demonstrate the effect of surficial pH reaction dependence, reaction steps R1-R3 in the model are replaced with SR1. Figure S4 below reproduces experimental results as shown in Fig. 3 of the main text while comparing model output using step SR1 instead of R1-R3 (simulation results given in dashed lines). Here, a pH dependence is still observed between basic and neutral/acidic conditions due to sensitivity of reaction steps R6-R9 in the main text. However, this dependence in the secondary chemical pathways of I^- fails to reproduce the kinetics observed in the experiment.
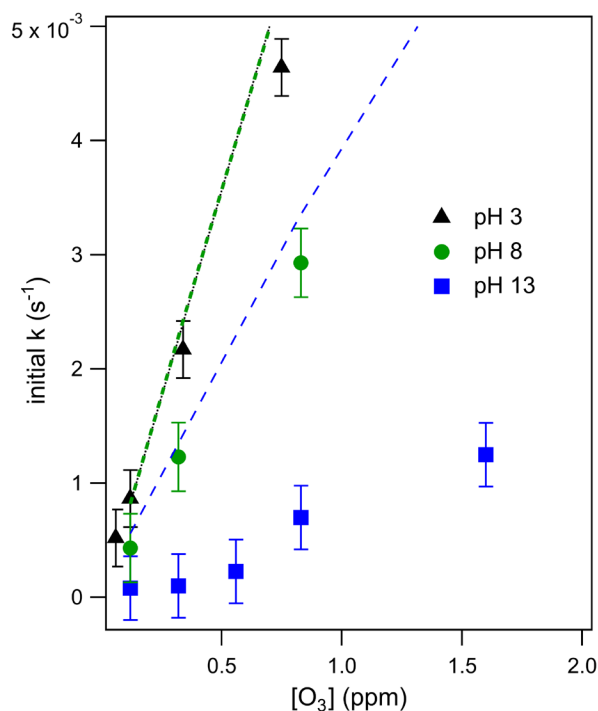

Fig. S10: Results of pH-dependence sensitivity test. Kinetics from Fig.3 in the main text are reproduced along with simulation results (dashed lines) obtained by replacing steps R1-R3 in the model with a single bimolecular reaction step $I^- + O_3$ with rate coefficient $k = 1.2 \times 10^9$ M^{-1} s^{-1}. Model output under these conditions overpredicts all observed kinetics and lacks sensitivity to pH between pH 3 and pH 8.

SI-7: Simulated Product Distributions

Example simulation kinetics are provided in Fig. S11 to demonstrate the difference in modeled oxidation product distributions across droplet pH for an example ozone concentration of $[O_3] = 820$ ppb. For droplet solutions with pH 3 and pH 8, I_2 is the major emission product with a fraction of HOI also emitted. Iodide conversion to HOI is seen to increase slightly as $[I^-]$ decreases. This is due to the reactive timescale of HOI conversion to I_2 becoming longer with decreasing $[I^-]$, allowing the evaporative channel

of HOI to become more significant. In strongly basic solution, IO_3^- is the main product, with close to 100% conversion. As mentioned in section SI-2 and in Fig. S3, the simulated product kinetics under pH 13 differ from what is observed in experiment, where the yield of IO_3^- appears to decrease with decreasing $[O_3]$. While the origin of the observation is not clear, potential coupling between the surface-solvation lifetimes of HOI/IO^- and I_2, their respective chemical lifetimes, and evaporation rates may lead to unexpected changes in mechanism for lower $[O_3]$.
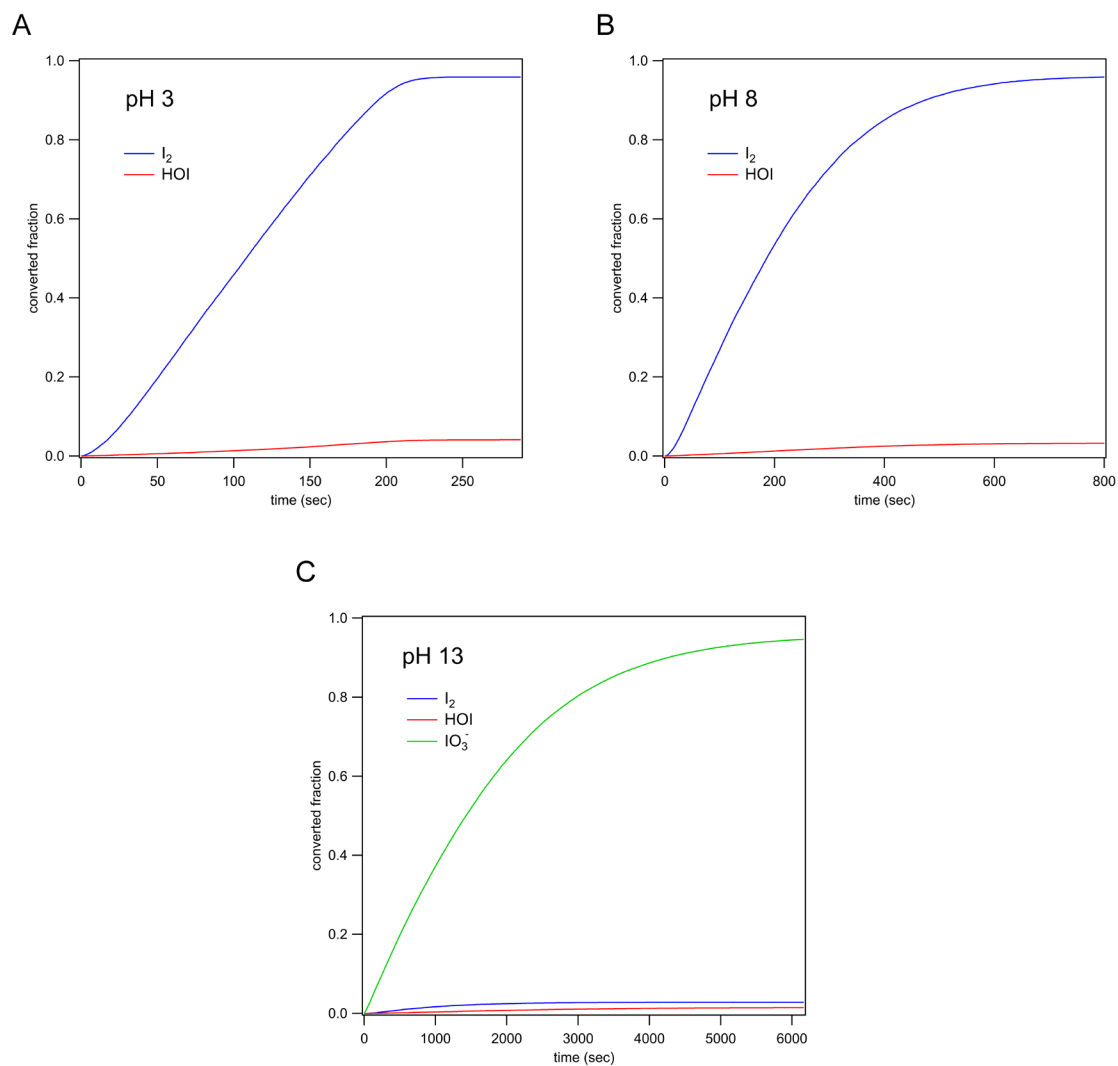
Fig. S11: Product distribution from three example simulations for pH 3, 8, and 13 labeled in panels A, B, and C, respectively. Example simulations are run using $[O_3]$ = 820 ppb. For pH conditions below the pKa of HOI (10.8), no IO_3^- is observed in solution and only volatile products remain. For both pH 3 and pH 8, I_2 is dominate with a small fraction of HOI emitted. For pH 13, IO_3^- dominates the overall products. As mentioned in the main text and section SI-5, volatile products for pH 13 are observed to increase in overall fraction with decreasing $[O_3]$.

Supplementary Reference:

(1) Jungwirth, P.; Tobias, D. J. Ions at the Air/Water Interface. *J. Phys. Chem. B* **2002**, *106* (25), 6361–6373. https://doi.org/10.1021/jp020242g.

(2) Woods, E.; Konys, C. A.; Rossi, S. R. Photoemission of Iodide from Aqueous Aerosol Particle Surfaces. *J. Phys. Chem. A* **2019**, *123* (13), 2901–2907. https://doi.org/10.1021/acs.jpca.8b12323.

(3) Liu, Q.; Schurter, L. M.; Muller, C. E.; Aloisio, S.; Francisco, J. S.; Margerum, D. W. Kinetics and Mechanisms of Aqueous Ozone Reactions with Bromide, Sulfite, Hydrogen Sulfite, Iodide, and Nitrite Ions. *Inorg. Chem.* **2001**, *40* (17), 4436–4442. https://doi.org/10.1021/ic000919j.

(4) Bhujel, M.; L. Marshall, D.; T. Maccarone, A.; I. McKinnon, B.; J. Trevitt, A.; Silva, G. da; J. Blanksby, S.; J. Poad, B. L. Gas Phase Reactions of Iodide and Bromide Anions with Ozone: Evidence for Stepwise and Reversible Reactions. *Phys. Chem. Chem. Phys.* **2020**, *22* (18), 9982–9989. https://doi.org/10.1039/D0CP01498B.

(5) Paquette, J.; Wren, J. C.; Sunder, S.; Ford, B. L. *The Disproportionation of Iodine (I)*; 0-7058-1073–9; United Kingdom, 1986; pp 29–45.

(6) Bichsel, Y.; von Gunten, U. Oxidation of Iodide and Hypoiodous Acid in the Disinfection of Natural Waters. *Environ. Sci. Technol.* **1999**, *33* (22), 4040–4045. https://doi.org/10.1021/es990336c.

(7) Lengyel, I.; Epstein, I. R.; Kustin, K. Kinetics of Iodine Hydrolysis. *Inorg. Chem.* **1993**, *32* (25), 5880–5882. https://doi.org/10.1021/ic00077a036.

(8) Sebők-Nagy, K.; Körtvélyesi, T. Kinetics and Mechanism of the Hydrolytic Disproportionation of Iodine. *Int. J. Chem. Kinet.* **2004**, *36* (11), 596–602. https://doi.org/10.1002/kin.20033.

(9) Palmer, D. A.; Ramette, R. W.; Mesmer, R. E. Triiodide Ion Formation Equilibrium and Activity Coefficients in Aqueous Solution. *J. Solut. Chem.* **1984**, *13* (9), 673–683. https://doi.org/10.1007/BF00650374.

(10) Sanemasa, I.; Kobayashi, T.; Piao, C. Y.; Deguchi, T. Equilibrium Solubilities of Iodine Vapor in Water. *Bull. Chem. Soc. Jpn.* **1984**, *57* (5), 1352–1357. https://doi.org/10.1246/bcsj.57.1352.

(11) Lin, C.-C. Volatility of Iodine in Dilute Aqueous Solutions. *J. Inorg. Nucl. Chem.* **1981**, *43* (12), 3229–3238. https://doi.org/10.1016/0022-1902(81)80094-2.

(12) Dunlop, P. J.; Stokes, R. H. The Diffusion Coefficients of Sodium and Potassium Iodides in Aqueous Solution at 25°1. *J. Am. Chem. Soc.* **1951**, *73* (11), 5456–5457. https://doi.org/10.1021/ja01155a520.

(13) Darrall, K. G.; Oldham, G. The Diffusion Coefficients of the Tri-Iodide Ion in Aqueous Solutions. *J. Chem. Soc. Inorg. Phys. Theor.* **1968**, 2584. https://doi.org/10.1039/j19680002584.

(14) Gregory, D. P.; Riddiford, A. C. 731. Transport to the Surface of a Rotating Disc. *J. Chem. Soc. Resumed* **1956**, 3756. https://doi.org/10.1039/jr9560003756.

(15) Gottschalk, C.; Libra, J. A.; Saupe, A. *Ozonation of Water and Waste Water: A Practical Guide to Understanding Ozone and Its Applications*, 2nd Edition.; Wiley-VCH Verlag GmbH & Co., 2010.

(16) Lamoureux, G.; Harder, E.; Vorobyov, I. V.; Roux, B.; MacKerell Jr, A. D. A Polarizable Model of Water for Molecular Dynamics Simulations of Biomolecules. *Chem Phys Lett* **2006**, *418* (1–3), 245–249.

(17) Miller III, T.; Eleftheriou, M.; Pattnaik, P.; Ndirango, A.; Newns, D.; Martyna, G. Symplectic Quaternion Scheme for Biophysical Molecular Dynamics. *J Phys Chem* **2002**, *116* (20), 8649–8659.

(18) Lopes, P. E.; Roux, B.; MacKerell, A. D. Molecular Modeling and Dynamics Studies with Explicit Inclusion of Electronic Polarizability: Theory and Applications. *Theor Chem Acc* **2009**, *124*, 11–28.

(19) Lamoureux, G.; Roux, B. Modeling Induced Polarization with Classical Drude Oscillators: Theory and Molecular Dynamics Simulation Algorithm. *J Chem Phys* **2003**, *119* (6), 3025–3039.

(20) Vieceli, J.; Roeselová, M.; Potter, N.; Dang, L. X.; Garrett, B. C.; Tobias, D. J. Molecular Dynamics Simulations of Atmospheric Oxidants at the Air−Water Interface: Solvation and Accommodation of OH and O3. *J. Phys. Chem. B* **2005**, *109* (33), 15876–15892. https://doi.org/10.1021/jp051361+.

(21) Dang, L. X. Computational Study of Ion Binding to the Liquid Interface of Water. *J. Phys. Chem. B* **2002**, *106* (40), 10388–10394. https://doi.org/10.1021/jp021871t.

(22) Frenkel, D.; Smit, B. *Understanding Molecular Simulation: From Algorithms to Applications*; Elsevier, 2001.

(23) Noskov, S. Y.; Lamoureux, G.; Roux, B. Molecular Dynamics Study of Hydration in Ethanol-Water Mixtures Using a Polarizable Force Field. *J Phys Chem B* **2005**, *109* (14), 6705–6713.

(24) Pollock, E.; Glosli, J. Comments on P3M, FMM, and the Ewald Method for Large Periodic Coulombic Systems. *Comput. Phys Comm* **1996**, *95* (2–3), 93–110.

(25) Dodin, A.; Geissler, P. L. Symmetrized Drude Oscillator Force Fields Improve Numerical Performance of Polarizable Molecular Dynamics. *J. Chem. Theory Comput.* **2023**, *19* (10), 2906–2917. https://doi.org/10.1021/acs.jctc.3c00278.

(26) Torrie, G. M.; Valleau, J. P. Nonphysical Sampling Distributions in Monte Carlo Free-Energy Estimation: Umbrella Sampling. *J Comput Phys* **1977**, *23* (2), 187–199.

(27) Kumar, S.; Rosenberg, J. M.; Bouzida, D.; Swendsen, R. H.; Kollman, P. A. The Weighted Histogram Analysis Method for Free-Energy Calculations on Biomolecules. I. The Method. *J Comput Chem* **1992**, *13* (8), 1011–1021.

(28) Farago, O.; Grønbech-Jensen, N. Fluctuation–Dissipation Relation for Systems with Spatially Varying Friction. *J. Stat. Phys.* **2014**, *156* (6), 1093–1110. https://doi.org/10.1007/s10955-014-1045-4.